

DYNAMIC MODELING AND SYSTEM IDENTIFICATION FOR A MMAM CONTROLLED FLEXIBLE MANIPULATOR

Yoonsu Nam

Stability and Control Lab., Agency for Defense Development

ABSTRACT

For a high bandwidth, accurate end of arm motion control with good disturbance rejection, the Momentum Management Approach to Motion control (MMAM) is proposed. The MMAM is a kind of position control technique that uses inertial forces, applied at or near the end of arm to achieve high bandwidth and accuracy in movement and in the face of force disturbances.

To prove the concept of MMAM, the end point control of a flexible manipulator is considered. For this purpose, a flexible beam is mounted on the x-y table, and the MMAM actuator is attached on the top of the flexible beam. A mathematical model is developed for the flexible beam being controlled by the MMAM actuator and slide base DC motor. A system identification method is applied to estimate some system parameters in the model which can not be determined because of the complexity of the mechanism. For the end point control of the flexible beam, the optimal linear output feedback control is introduced.

INTRODUCTION

Lightweight manipulators suffer because they are unable to attain high bandwidth position control, or to maintain position in the face of high bandwidth disturbing forces. This is inherent in any manipulator where the driving actuator is separated from the end of arm by a structure which deflects significantly during the motion.

Alternate approaches to resolving these problems are

1. augmenting the arm with additional fine motion device (micro-manipulator) on the end-effector to achieve high positional accuracy and variable compliance without moving the entire structure [1,2],
2. active control of the flexible modes of the structure to reduce the effects of deflections by using a control algorithm that specifically accounts for the deflections [3-5],
3. bracing against some object near the end-effector to enhance accuracy and to bear the interaction force between the end-effector and the environment [6],
4. more efficient structures which achieve better performance per unit weight by using (a) stiffer materials, (b) more efficient geometries, e.g. closed chains, or (c) passive damping [7],
5. momentum management approach to motion control (MMAM) which uses momentum exchange between the manipulator end of arm and one or more proof-mass(es) near the tip of a manipulator [8,12].

The approach using micro-manipulators is excellent where rapid positioning of very light payloads is required. If the payload is heavy, the forces required to move the payload rapidly are such that a motion of the micro-manipulator results more in bending and vibration of the arm than motion of the payload. Similarly, if there are high bandwidth disturbing forces, these are transmitted to the arm. A way of countering that, a bracing strategy, has been suggested which may be quite practical when there is a convenient place to brace.

A momentum management approach to the motion control (MMAM) has been suggested for overcoming this shortcoming. MMAM refers to momentum exchange between the manipulator end of arm and one or more proof mass(es) near the tip of a manipulator. External disturbance force on the end effector is temporally transferred to the proof mass(es) in order to maintain the end point desired position. This momentum is subsequently absorbed by the manipulator structure through the proper control of the main servo system. Momentum management has also been used in space applications to control the attitude of a space craft [10]. The use of MMAM to control the position of a robot, machine tool, or conventional motion control system does not seem to have been addressed earlier.

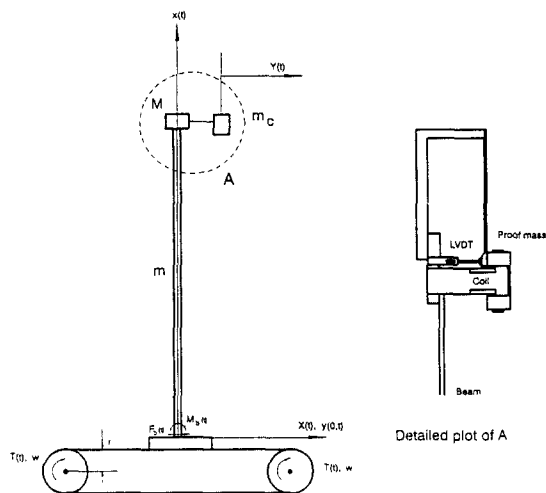


Fig. 1 Schematic of experimental setup

DESCRIPTION OF EXPERIMENTAL SETUP

Fig. 1 shows the schematic of the experimental setup and MMAM device. A flexible beam is clamped on the slide base of x-y table. The flexible beam, which has the length of 28.5 inches, the thickness of 1/8 inches, and the width of 1.5 inches, is made of aluminum. The table is driven by two identical DC motors, and has a chain mechanism to position the slide base. These DC motors are separately located at both ends of the chain drive as shown in Fig. 1. Each DC motor has a gear box with the reduction ratio of 65.5 : 1.

On the top of a beam, the MMAM device is mounted. The MMAM device is composed of a coil and permanent magnet (called proof mass). This coil is fixed on the beam so that the generated magnetic force could be transferred to an end point of a beam directly, and the permanent magnet is attached through a flexure spring to the beam. The DC motor of the x-y table and the MMAM device are each driven by a current control type linear bipolar amplifier.

An optical encoder attached on the DC motor axis is used for the measurement of the slide base displacement. The acceleration and position of the end point of the flexible beam are sensed by an accelerometer and machine vision. To measure the relative displacement between the flexible beam end point and the proof mass, an LVDT (Linear Variable Differential Transformer) is used.

MATHEMATICAL MODELING

The Euler-Bernouli beam model, in which shear deformation and rotary inertia effects are ignored, is used for the flexible beam. Then, the motion of a flexible beam is governed by the equation of

$$m \frac{\partial^2 y(x, t)}{\partial t^2} + EI \frac{\partial^4 y(x, t)}{\partial x^4} = 0 \quad (1)$$

with the boundary condition of

$$\begin{aligned} y(0, t) &= 0 \\ \frac{\partial y}{\partial x}(0, t) &= 0 \\ \frac{\partial^2 y}{\partial x^2}(L, t) &= 0 \\ M \frac{\partial^2 y}{\partial t^2}(L, t) &= -\left\{ -EI \frac{\partial^3 y}{\partial x^3}(L, t) \right\} \end{aligned} \quad (2)$$

where m = mass per unit length of beam
 M = concentrated mass on the top of beam
 L = length of the beam

The solution of Eq. (1) is given as

$$y(x, t) = \sum_{i=1}^{\infty} \phi_i(x) q_i(t) \quad (3)$$

where

$$\begin{aligned} q_i(t) &= i\text{-th generalized coordinate} \\ \phi_i(x) &= c_i \{ \sin \beta_i x - \sinh \beta_i x - \gamma_i (\cos \beta_i x - \cosh \beta_i x) \} \\ \gamma_i &= \frac{\sin \beta_i L + \sinh \beta_i L}{\cos \beta_i L + \cosh \beta_i L} \end{aligned} \quad (4)$$

By the boundary conditions of Eq. (2), each \mathcal{J}_i has to meet the frequency equation of [11]

$$\frac{M}{m} \beta (\cos \beta L \sinh \beta L - \sin \beta L \cosh \beta L) + 1 + \cos \beta L \cosh \beta L = 0 \quad (5)$$

By using the orthonormality condition of

$$m \int_0^L \phi_i(x) \phi_j(x) dx + M \phi_i(L) \phi_j(L) = \delta_{ij} \quad (6)$$

and considering the exciting force terms by the MMAM device and the movement of slide base, the generalized coordinate $q_i(t)$ must satisfy the following equation of

$$\ddot{q}_i(t) + \omega_i^2 q_i(t) = \phi_i(L) f(t) - \frac{d^2 X}{dt^2} \left\{ m \int_0^L \phi_i(x) dx + M \phi_i(L) \right\} \quad (7)$$

where $f(t)$ is the generated force by MMAM $\frac{d^2 X}{dt^2}$ is the acceleration of the slide base.

It is generally sufficient to approximate the end point displacement $y(L,t)$ by including only 2 or 3 terms in Eq. (3)

$$y(L,t) \cong \sum_{i=1}^{2(\text{or } 3)} \phi_i(L) q_i(t) \quad (8)$$

Fig. 2 is the block diagram representation of Eq. (7) and (8).

The effect of MMAM actuator

The block diagram of Fig. 3 shows the dynamics of a beam end point, $y(L,t)$, and the proof mass displacement, $Y(t)$, for the input voltage to the coil of MMAM actuator. The inner loops represent the flexure spring force, and damping effect, and outer loop is caused by the back EMF of the MMAM actuator. The system parameters of Fig. 3 are listed on Table 1. Some system parameters are measured directly, and others (superscripted with * in Table 1) are determined by the system identification method explained in the next section. The transfer function of the acceleration, $\ddot{y}(L,t)$, from the input voltage, V_m , is given by

$$\frac{\ddot{y}(L,t)}{V_m} = \frac{-C_1 \frac{K_m}{R} q(s)^2}{p(s) \left\{ s^2 + \frac{C_1}{m_c} \left(\frac{K_m K_m}{R} + B_1 \right) s + \frac{C_1 B_1}{m_c} \right\} + C_1 q(s) \left\{ \left(\frac{K_m K_m}{R} + B_1 \right) s + K_1 \right\}} \quad (9)$$

where $\frac{q(s)}{p(s)} = \sum_{i=1}^3 \frac{\phi_i(L) s^2}{s^2 - \omega_i^2}$

Table 1 System parameters in Fig. 3

System parameter	Description	Value	Unit
R_1	resistance of coil	4	ohm
K_{c1}^*	back EMF constant	0.061441	V/(in/sec)
K_{f1}^*	force constant	0.54376	lb/A
K_s^*	flexure spring constant	0.68771	lb/inches
B_1^*	damping constant	1.8072×10^{-2}	lb/(in/sec)
m_c	mass of permanent magnet	0.6614	lb _m
C_1	conversion factor	386.4	(in/sec ²)/g
L	length of beam	29	inches
m	mass/unit length of beam	1.8338×10^{-2}	lb _m /inches
M	concentrated mass	0.4852	lb _m

Fig. 4 is Bode plot of the transfer function of Eq. (9). There are four peaks. The second peak is caused by the resonance of the MMAM actuator (i.e. by the flexure spring and proof mass). The remaining peaks are from 3 modal frequencies of the beam. The point designated by 'x' is the measured acceleration of a beam end point for the input voltage to the MMAM actuator at each exciting frequency. The discrepancy between the analytic and experimental results becomes larger for the high modal frequencies. One of the reasons of this difference comes from the mounting mechanism of the system on the Aluminum base plate. Fig. 4 shows the experimental data match well with the analytical results up to the second modal frequency.

The effect of the movement of slide base

As shown in Fig. 1, the flexible beam is clamped on the slide base. Therefore, the shear force, $F_b(t)$,

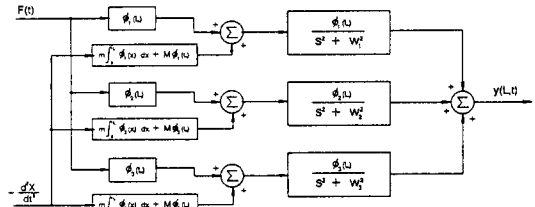


Fig. 2 Block diagram of beam dynamics

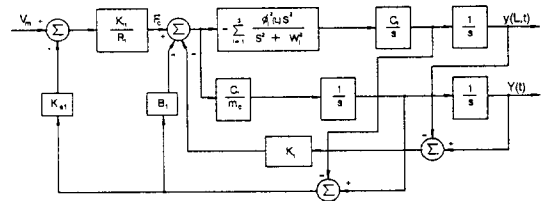


Fig. 3 Block diagram of MMAM actuator effect

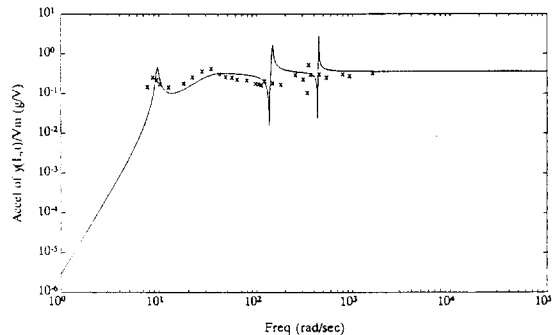


Fig. 4 Frequency response of the end point acceleration for V_m

and bending moment, $M_b(t)$, at a clamping point caused by a beam deflection must be considered on the dynamics of the slide base. The differential equation for a motor rotation is given by

$$J\dot{\omega}(t) + B_2\omega = T(t) + \frac{1}{N}\{M_b(t) + rF_b(t)\} \quad (10)$$

where

$$M_b(t) = EI \sum_{i=1}^n \phi_i''(0)q_i(t)$$

$$F_b(t) = -EI \sum_{i=1}^n \phi_i'''(0)q_i(t)$$

and J is total moment of inertia on the motor axis, N is gear reduction ratio, and $T(t)$ is the developed torque by the motor.

By combining Eq. (7), Eq. (10) and DC motor characteristic, the block diagram of Fig. 5 is constructed. The system parameters in Fig. 5 are shown on Table 2. Again, some parameters (superscripted with * in Table 2) are found from the parameter identification method. The resulting transfer function of the slide base displacement, X , and the end point acceleration, $\ddot{y}(L,t)$, from the input voltage of the DC motor is given by

$$\frac{X}{V_b} = \frac{\frac{C_3 K_{e2}}{R_2} p_1(s)}{s p_1(s)(Js + C_2 B_2 + \frac{K_{e2}}{R_2}) + C_2 C_3 s^2 q_1(s)} \quad (11)$$

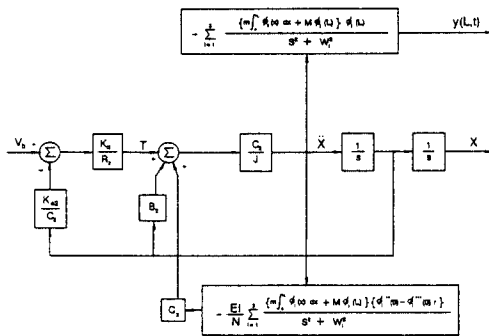


Fig. 5 Block diagram of slide base dynamics

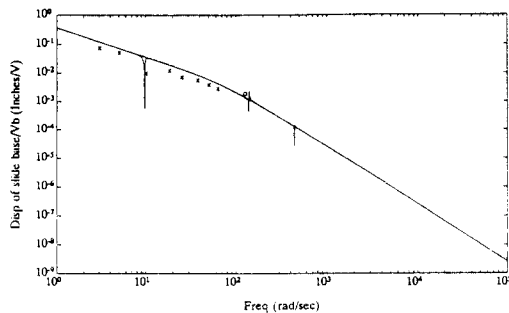


Fig. 6 Frequency response of slide base displacement for V_b

Table 2 System parameters in Fig. 5

System parameter	Description	Value	Unit
R_2	resistance	8.2	ohm
K_{e2}	back EMF constant	0.0388	V/(r/sec)
K_{t2}	torque constant	5.50	oz-in/A
B_2^*	damping ratio	0.46464	oz-in/in-sec
r	radius of chain	1.5	inches
I	area moment of inertia	2.4414×10^{-4}	in ⁴
E	Young's modulus of Al	10.5×10^6	lb _r /in ²
N	reduction ratio	76.4385	-
J^*	moment of inertia	9.5206×10^{-4}	oz-in ²
C_2	conversion factor	1.8571×10^{-2}	in/rad
C_3	conversion factor	.6	lb _r /oz _r

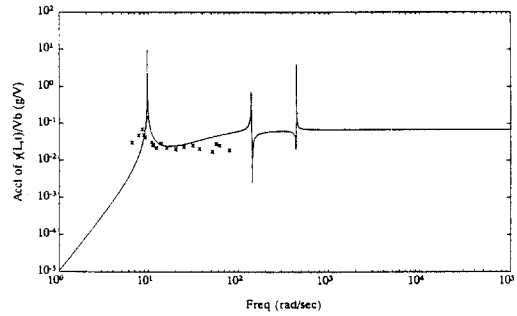


Fig. 7 Frequency response of the end point acceleration for V_b

$$\frac{\ddot{y}(L,t)}{V_b} = \frac{\frac{C_3 K_{e2}}{R_2} s p_1(s) q_2(s)}{p_1(s) p_2(s) (Js + C_2 B_2 + \frac{K_{e2}}{R_2}) + C_2 C_3 s q_1(s) p_2(s)} \quad (12)$$

where

$$q_1(s) = \frac{EI}{N} \sum_{i=1}^3 \frac{\{\phi_i'(0) - \phi_i''(0)r\} \{m \int_0^L \phi_i(x) dx\}}{s^2 + \omega_i^2}$$

$$q_2(s) = \frac{EI}{N} \sum_{i=1}^3 \frac{\phi_i(L) \{m \int_0^L \phi_i(x) dx\} s^2}{s^2 + \omega_i^2}$$

Fig. 6 is the Bode plot for Eq. (11). The solid line in Fig. 6 represents the Bode plot of this transfer function, and dashed line the Bode plot of the same transfer function, when the influence of the beam deflection forces (i.e. $F_b(t)$ and $M_b(t)$) are ignored. The points 'x' are the measured displacement of the slide base. Based on the experimental observation, there is no response of the slide base beyond 20 Hz of the driving signal, even though the maximum input voltage (10 V) was applied to the DC motor.

The Bode plot of the transfer function of the end point acceleration, $\ddot{y}(L,t)$, for the base DC motor driving voltage, V_b , is shown as solid line in Fig. 7. Again, the dotted line represents the same transfer function, when the effect of a flexible beam deflection on the dynamics of the slide base is ignored. The measured end point acceleration is also shown as the mark 'x'. Because of the dead response of the slide base for the driving signals above 20 Hz due to the backlash, the second and third mode frequency could not be measured.

SYSTEM PARAMETER IDENTIFICATION

The modeling of a flexible beam dynamics is completed mathematically. Some system parameters such as the mass of the permanent magnet (m_c), the resistance of the coil (R_1)... can be easily measured, but others such as a flexure spring constant (K), force constant (K_{t1}) of the MMAM actuator... can not. By collecting the system input-output data, and using the system identification method, those unknown system parameters in the MMAM actuator and slide base moving mechanism are estimated.

There are a number of well known parameter estimation techniques that have been successfully applied to the identification problem. They include the methods of maximum likelihood, least square, cross correlation, instrumental variable, and stochastic approximation. But, in this application, the least square method is selected. For the identification of the MMAM actuator and slide base mechanism, three parametric models, which are ARX (AutoRegressive with eXogenous variables), ARMAX (AutoRegressive Moving Average with eXogenous variables), and OE (Output Error) model, are chosen.

Ideally, the impulse function, which has a flat power spectrum, is the best input signal for the system identification, because the system is excited by a wide spectrum of frequencies. But, one of the practical optimum input signal is the so-called pseudo-random binary sequence (PRBS) [11], which is a band-limited white noise sequence. To avoid the aliasing phenomenon, this PRBS period T should be greater than the settling time of the system to be identified. The greater the magnitude of a PRBS is, the better the identification result, because a high power input means high signal to noise ratio at the system output. But, this magnitude should be chosen so as not to saturate the system output.

Identification of the MMAM actuator

The MMAM actuator, which is schematically described in Fig. 1, can be modelled as

$$\frac{Y(s)}{V_m(s)} = \frac{C_1 K_{t1} / (R_1 m_c)}{s^2 + (K_{t1} K_{e1} / R_1 + B_1) C_1 / m_c s + C_1 K_1 / m_c} \quad (20)$$

Again, the meaning of each system parameter is given on Table 2. If we use the z -transform representation, Eq. (20) is changed to

$$\frac{Y(z)}{V_m(z)} = \frac{b_1 z^{-1} + b_2 z^{-2}}{1 + a_1 z^{-1} + a_2 z^{-2}} \quad (21)$$

The numerical values of the coefficients in Eq. (21) depend on the sampling time interval.

As mentioned before, the system parameters in Eq. (20) except the mass of a permanent magnet (m_c), and the resistance of a coil (R_1) can not be easily measured. But, by using the system identification method, the coefficients in Eq. (20) can be estimated. Then, by converting this estimated z -transform into the Laplace transform, and matching the coefficients of this converted s -transform with that of Eq. (20), these unknown system parameters can be determined.

The experimental setup is depicted in Fig. 8. The PRBS, which has the alternating magnitude of -1.0V and 1.0V excites the MMAM actuator. The disturbed proof mass displacement is measured using LVDT, and recorded on the RAM of MC68020 micro-computer. The sampling time of this experiment is 2 msec. The experimental data are sampled during 8 seconds. These input-output data are uploaded to the IBM-PC for the analysis. The MATLAB system identification software package is used for the manipulation of these data.

Among the uploaded experimental input-output data, the first 1000 data points, which amount to the data of the first 2 seconds, are selected for building a model. The remaining data are used in testing the accuracy of the model. A simple model evaluation is done by running a simulation that real input data are fed into the model, and comparing the simulated output with the actual, measured output. Fig. 9, Fig. 10, and Fig. 11 represent this result of the model evaluation for the parametric model of ARX, ARMAX, and OE for the time interval from 2 to 8 seconds. The initial discrepancies between the experimental data and the model output in these figures are due to the transient responses of the each model due to the wrong initial conditions of the model. As shown clearly in Fig. 9, the identification result of

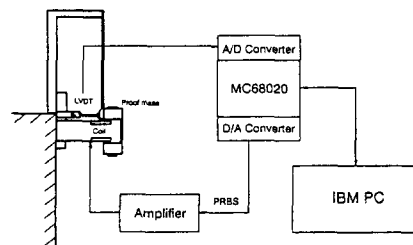


Fig. 8 Experimental setup for identification of MMAM

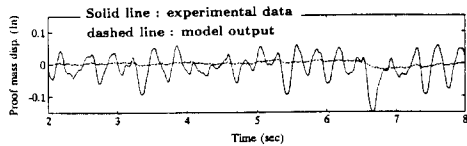


Fig. 9 ARX model evaluation for MMAM actuator

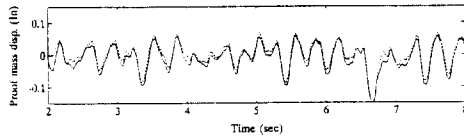


Fig. 10 ARMAX model evaluation for MMAM actuator

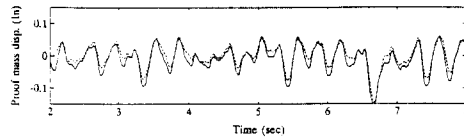


Fig. 11 OE model evaluation for MMAM actuator

the ARX model is the worst among the three models. The OE model of Fig. 11 is slightly better than the ARMAX model of Fig. 10 in reproducing the experimental data. Therefore, the OE model is chosen in identifying the coefficients in Eq. (21). Again, these coefficients are used for the determination of the system parameters in Eq. (20). Those numerical values are shown on Table 1.

Identification of the slide base mechanism

The same procedures as that of identifying the MMAM actuator dynamics were taken for the slide base moving mechanism. Therefore, only the experimental data are described here. Fig. 12, Fig. 13, and Fig. 14 show the results of the model output of ARX, ARMAX, and OE with the actual response of the slide base. As shown in Fig. 12, the ARX model output gives the best fit to the experimental data among the three models. Therefore, the system parameters of the slide base mechanism were determined based on the ARX model. The numerical values of these parameters are shown on Table 2.

The system identification process was successfully applied to the estimation of the system parameters in the MMAM actuator and slide base moving mechanism. The output of each parametric identification model matched well with the observed system output except for the case of Fig. 9. The reason for this discrepancy between the model output and observed output in Fig. 9 is considered as the result of low signal to noise ratio(S/N ratio) in the measured output signal [12].

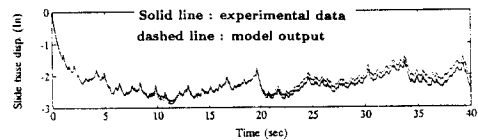


Fig. 12 ARX model evaluation for slide base mechanism

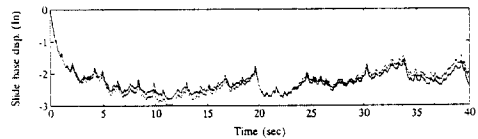


Fig. 13 ARMAX model evaluation for slide base mechanism

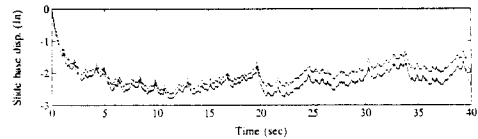


Fig. 14 OE model evaluation for slide base mechanism

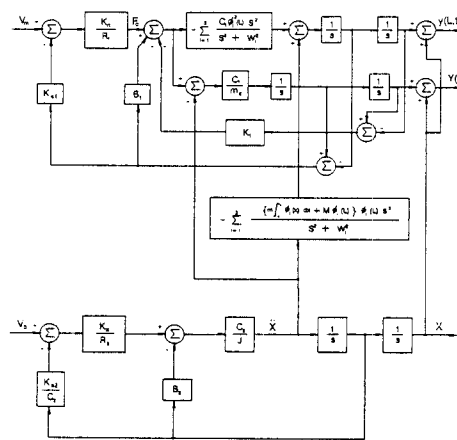


Fig. 15 Block diagram of simplified model

In conclusion, the modeling of the whole system can be described by the block diagram of Fig. 15. To evaluate the accuracy of the model, several experiment are made. It is shown in the Fig. 4, Fig. 6 and Fig. 7 that these experimental data match well with the analytic results.

THE SIMULATION - DISTURBANCE REJECTION

One of the advantages of using MMAM is that it has the property of a good disturbance rejection. when there is a disturbance force at the end of a beam. To demonstrate this characteristic, it is assumed there is an impulse type disturbance force on the beam end point.

The performance of the optimal linear state feed-

back system depends on the choice of weighting matrix Q for the state variables and R for the inputs. However, there is no systematic way to select these matrices, except for iteratively changing the values of the matrices with some intuitions of a designer to reach at a satisfactory result. After a lot of simulations, the following performance index was chosen.

$$PI = \sum_{k=0}^{\infty} \{ \underline{y}(k)^T Q \underline{y}(k) + \underline{u}(k)^T R \underline{u}(k) \} \quad (22)$$

$$= \sum_{k=0}^{\infty} \{ q_1 \dot{y}(k)^2 + q_2 (Y(k) - y(k))^2 + q_3 \dot{y}(k)^2 + r_1 V_m(k)^2 + r_2 V_b(k)^2 \}$$

In Eq. (22), $y(k)$, $\dot{y}(k)$, $Y(k)$, $V_b(k)$, and $V_m(k)$ represents the displacement of the beam end point, its velocity, displacement of the proof mass, and control inputs for the base DC motor and MMAM actuator respectively.

For the value of $q_1 = q_2 = q_3 = r_1 = 1$ and $r_2 = 10^{-2}$, Fig. 16 shows the impulse response of the beam end point, velocity, relative displacement of the proof mass, and slide base movement. Values of Q and R matrix were selected based on the consideration of the limited working ranges of the proof mass, and slide base actuator saturation characteristic. Because of the impact force, the end point velocity momentarily has the initial value of 2.8 inches/sec. The maximum displacement of the beam end point is about 0.065 inches for the impulse disturbance. To compensate the motion of the end point, the proof mass moves to the positive direction (outward), and returns to its neutral position after the impact.

CONCLUSION

The concept of MMAM was applied to the end point control of a flexible manipulator. A linear mathematical model is developed for the flexible beam controlled by MMAM actuator and slide base DC motor. A system identification method is applied to estimate some system parameters which can not be measured. To evaluate the accuracy of a model, the frequency

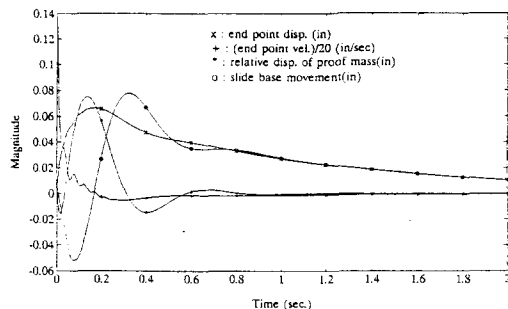


Fig. 16 impulse response of a MMAM controlled flexible beam

response of the beam dynamics has been determined experimentally, and compared with the analytic result. Simulation result for the disturbance rejection is presented to show the capability of MMAM.

REFERENCES

1. Sharon, A. and Hardt, D., "Enhancement of Robot Accuracy Using End Point Feedback and a Macro-Micro Manipulator System", American Control Conference Proc., San Diego, CA, June 6- 8, 1984, pp 1836- 1842
2. Hollis, R.L., "A Six Degree of Freedom Magnetically Levitated Variable Compliance Fine Motion Wrist", 4th Int. Symposium for Robotic Research, Santa Kruz, CA, August 8- 14, 1987
3. Cannon Jr., R.H. and Schmitz, E., "Initial Experiments on the End Point Control of a Flexible One Link Robot", Int. J. Robotic Research, 3(3), 1984, pp 62- 75
4. Kanoh, H. and Lee, H.G., "Vibration Control of One Link Flexible Arm", Proc. 24th Conference on Decision and Control, Ft. Laderdale, FL, Dec. 1985, pp 1172- 1177
5. Hasting, G.G. and Book, W.J., "Experiments in Optimal Control of a Flexible Arm", Proc. 1985 American Control Conference, June, 1985, pp 728- 729
6. Book, W.J., Le, S. and Sangveraphunsiri, V., "Bracing Strategy for Robot Motion", Proc. of RoManSy' 84: the 5th CISM-IFTToMM Symp. on Theory and Practice of Robots and Manipulator, Udine, Italy, June 1984, pp 179- 185
7. Albert, T., "Augmenting the Control of a Flexible Manipulator with Passive Mechanical Damping", Ph. D. Thesis, Georgia Tech, Mechanical Eng., Sept. 1986
8. Dickerson, S.L. and Nam, Y.S., "Milling with Compliant Machine", 1988 USA- Japan Symposium of Flexible Automation, July 1988
9. Ham, F.M. and Greeley, S.W., "Active Damping Control Design for the Mast Flight System", Proc. American Control Conference Vol. 1., 1987, pp 355- 367
10. Meirovitch, L., "Elements of Vibration Analysis", McGraw- Hill Book Company 1986
11. Ljung, L., "System Identification : Theory for the User", Prentice- Hall, 1987
12. Nam, Y.S., "Momentum Management for the End Point Control of a Flexible Manipulator". Ph. D. Thesis. Georgia Tech., Mechanical Eng., 1991